A Stochastic Ekman-Stokes Model for Coupled Ocean-Atmosphere-Wave Dynamics

Long Li[1,2], Etienne Mémin[1,2], and Bertrand Chapron[1,3]

[1] ODYSSEY Team, Centre Inria de l'Université de Rennes, France
[2] IRMAR – UMR CNRS 6625, Rennes, France
[3] Laboratoire d'Océanographie Physique et Spatiale, Ifremer, Plouzané, France
Corresponding author: Long Li, long.li@inria.fr

Abstract. Accurate representation of atmosphere-ocean boundary layers, including the interplay of turbulence, surface waves, and air-sea fluxes, remains a challenge in geophysical fluid dynamics, particularly for climate simulations. This study introduces a stochastic coupled Ekman-Stokes model (SCESM) developed within the physically consistent Location Uncertainty framework, explicitly incorporating random turbulent fluctuations and surface wave effects. The SCESM integrates established parameterizations for air-sea fluxes, turbulent viscosity, and Stokes drift, and its performance is rigorously assessed through ensemble simulations against LOTUS observational data. A performance ranking analysis quantifies the impact of different model components, highlighting the critical role of explicit uncertainty representation in both oceanic and atmospheric dynamics for accurately capturing system variability. Wave-induced mixing terms improve model performance, while wave-dependent surface roughness enhances air-sea fluxes but reduces the relative influence of wave-driven mixing. This fully coupled stochastic framework provides a foundation for advancing boundary layer parameterizations in large-scale climate models.

1 Introduction

Numerical modeling of geophysical fluid dynamics, particularly in climate systems, presents significant challenges due to the multi-scale nature of these systems and the complex nonlinear interactions that govern their behavior. Accurately simulating large-scale atmospheric and oceanic flows while maintaining computational efficiency requires the careful modeling or parameterization of subgrid-scale processes. Many of these processes are intermittent, nonlinear, and inherently random, underscoring the need for innovative approaches to represent uncertainties. As highlighted by Hasselmann [1976], Majda et al. [1999], Palmer [2019], stochastic modeling has emerged as a powerful tool for improving the representation of unresolved dynamics, thereby enhancing the accuracy of weather and climate predictions.

In this study, we adopt a physically consistent stochastic framework known as modeling under location uncertainty (LU), originally introduced by Mémin

[2014]. This approach preserves fundamental physical properties, such as energy conservation [Bauer et al., 2020], while naturally incorporating modeling errors and approximations to improve the representation of unresolved scales and their effects. A hierarchy of stochastic geophysical models has been systematically developed and validated within this framework, effectively capturing mesoscale and submesoscale dynamics within large-scale atmospheric and oceanic flows. Examples include the shallow water model [Brecht et al., 2021], the quasi-geostrophic model [Li et al., 2023], and the primitive hydrostatic model [Tucciarone et al., 2025]. By integrating stochasticity, LU-based models improve uncertainty representation and enable coarse-grid simulations to reproduce the long-term statistical properties of high-resolution reference flows.

The LU framework also advances stochastic formulations for wave-current and air-sea interactions by capturing the impact of unresolved small-scale fluctuations on large-scale dynamics. Bauer et al. [2020] demonstrates that wave-current interactions, including the Coriolis-Stokes and vortex forces in the Craik-Leibovich system, can be interpreted as statistical effects of unresolved flow inhomogeneity within a stochastic flow representation. Building on this, Li et al. [2024] introduces a stochastic model for the upper ocean Ekman boundary layer, incorporating unresolved velocity fluctuations, which lead to greater variability, increased kinetic energy, and more extreme events compared to standard models. Sensitivity analyses in that study highlight the influence of transient winds and surface waves, which enhance the dispersion of realizations while maintaining a balanced representation of errors. However, the model treats wind as a prescribed Gaussian process, neglecting its interaction with currents and waves and thereby failing to capture wave-modulated feedback on wind stress.

Expanding upon this foundation, the present work develops a fully coupled stochastic model that integrates turbulence, surface wave effects, and air-sea fluxes, explicitly capturing the interactions between random wind, waves, and currents. This one-dimensional vertical modeling approach is essential for realistic coarse-scale climate simulations, as it provides a physically consistent framework for parameterizing unresolved boundary layer turbulence and generating vertical profiles at the model's resolution grid points.

The paper is structured as follows: Section 2 describes the stochastic coupled Ekman-Stokes model (SCESM) and its parameterizations. Section 3 presents numerical results and comparisons with observational data. Finally, Section 4 concludes the study and discusses potential avenues for future research.

2 Models

In this section, we introduce the proposed stochastic framework for the coupled ocean-atmosphere Ekman layers, along with well-established parameterizations for air-sea fluxes, turbulent viscosity, and Stokes drift.

2.1 Stochastic formulation for air-sea coupled Ekman layers

As illustrated in Fig. 1, the vertical domain is decomposed as follows: the atmospheric boundary layer (ABL) is defined in $\Omega^a = [\delta^a, H^a]$ (with $\delta^a \sim 10$m and $H^a \sim 1000$m), the ocean boundary layer (OBL) is defined in $\Omega^o = [H^o, \delta^o]$ (with $\delta^o \sim -1$m and $H^o \sim -100$m), while the air-sea interface consists of the atmospheric surface boundary layer (ASBL) in $[0, \delta^a]$ and the ocean surface boundary layer (OSBL) in $[\delta^o, 0]$.

Following the derivation of the generalized stochastic Craik-Leibovich equations [Bauer et al., 2020] and the generalized stochastic Ekman-Stokes model [Li et al., 2024], we consider coupling two time-dependent Ekman models for the ABL and OBL. Hereafter, this will be referred to as the stochastic coupled Ekman-Stokes model (SCESM), described by the following stochastic partial differential equations:

$$\begin{aligned} \mathrm{d}\mathbf{u}^\alpha = &\Big(-if\big(\mathbf{u}^\alpha + \mathbf{u}_s^\alpha - \mathbf{u}_g^\alpha\big) + \partial_z\big(\nu^\alpha \partial_z(\mathbf{u}^\alpha + \mathbf{u}_s^\alpha)\big)\Big)\,\mathrm{d}t \\ &- \Big(\sigma_z^\alpha \partial_z\big(\mathbf{u}^\alpha + \mathbf{u}_s^\alpha\big) + if\boldsymbol{\sigma}_{\mathbf{x}}^\alpha\Big)\,\mathrm{d}B_t^\alpha, \qquad z \in \mathring{\Omega}^\alpha,\ t > 0, \end{aligned} \tag{2.1a}$$

$$\mathbf{u}^\alpha(z, 0) = \mathbf{u}_g^\alpha, \qquad z \in \mathring{\Omega}^\alpha, \tag{2.1b}$$

$$\mathbf{u}^\alpha(H^\alpha, t) = \mathbf{u}_g^\alpha, \qquad t > 0, \tag{2.1c}$$

$$\rho^\alpha \nu^\alpha \partial_z \mathbf{u}^\alpha(\delta^\alpha, t) = \boldsymbol{\tau}(t), \qquad t > 0. \tag{2.1d}$$

Here, $\alpha \in \{a, o\}$ denotes atmospheric and oceanic components, respectively. The variable $\mathbf{u}^\alpha(z,t) = u^\alpha(z,t) + iv^\alpha(z,t)$ represents the horizontal velocity in complex notation, with i as the imaginary unit. The geostrophic velocity component $\mathbf{u}_g^\alpha = u_g^\alpha + iv_g^\alpha$ is assumed time- and depth-independent. The Coriolis frequency is denoted by f. The viscosity coefficient is given by $\nu^\alpha(z,t) = \nu_m^\alpha + a_{zz}^\alpha(z,t)$, incorporating both molecular and turbulent effects. The uniform density is denoted by ρ^α, and $\boldsymbol{\tau}(t) = \tau_x(t) + i\tau_y(t)$ is the time-dependent surface wind stress.

In Eq. (2.1a), the term $\boldsymbol{\sigma}^\alpha\,\mathrm{d}B_t^\alpha = (\boldsymbol{\sigma}_{\mathbf{x}}^\alpha\,\mathrm{d}B_t^\alpha, \sigma_z^\alpha\,\mathrm{d}B_t^\alpha)$ represents a stochastic noise component originating from the Location Uncertainty (LU) framework [Mémin, 2014, Resseguier et al., 2017, Bauer et al., 2020], which accounts for unresolved turbulent motions probabilistically. The noise is spatially correlated through the correlation operator $\boldsymbol{\sigma}^\alpha$, acting on a cylindrical Brownian motion B_t^α. The turbulence-induced viscosity coefficient a_{zz}^α is linked to the Itô's quadratic variation process [Bauer et al., 2020]:

$$\frac{1}{2}\mathrm{d}\left\langle \int_0^\bullet \sigma_z^\alpha\,\mathrm{d}B_s^\alpha, \int_0^\bullet \sigma_z^\alpha\,\mathrm{d}B_s^\alpha \right\rangle_t = \frac{1}{2}\sigma_z^\alpha \sigma_z^\alpha\,\mathrm{d}t =: a_{zz}^\alpha\,\mathrm{d}t. \tag{2.2a}$$

The Itô-Stokes drift (introduced by Bauer et al. [2020]), $\mathbf{u}_s = \partial_z \boldsymbol{a}_{\mathbf{x}z}$ (within the Ekman layer scalings [Li et al., 2024]), captures the vertical inhomogeneity of co-quadratic variation between horizontal and vertical noise components:

$$\frac{1}{2}\mathrm{d}\left\langle \int_0^\bullet \boldsymbol{\sigma}_{\mathbf{x}}^\alpha\,\mathrm{d}B_s^\alpha, \int_0^\bullet \sigma_z^\alpha\,\mathrm{d}B_s^\alpha \right\rangle_t = \frac{1}{2}\boldsymbol{\sigma}_{\mathbf{x}}^\alpha \sigma_z^\alpha\,\mathrm{d}t =: \boldsymbol{a}_{\mathbf{x}z}^\alpha\,\mathrm{d}t. \tag{2.2b}$$

The above provides a general description of our stochastic model. To specify further the noise, we may also formulate the following inverse problem: determining a specific noise such that the resulting statistical properties correspond to a prescribed turbulent viscosity a^{α}_{zz} and a given Stokes drift $\mathbf{u}^{\alpha}_{s}$.

Given the turbulent viscosity a^{α}_{zz}, we adopt the following spectral decomposition for the vertical noise component:

$$\sigma^{\alpha}_{z}\,\mathrm{d}B^{\alpha}_{t} = \sqrt{2}\sum_{n>0}\big[(a^{\alpha}_{zz})^{1/2}, e^{\alpha}_{n}\big](t)\, e^{\alpha}_{n}(z)\,\mathrm{d}\beta^{\alpha}_{n}(t), \tag{2.3a}$$

where $\{e^{\alpha}_{n}\}$ denotes a set of localized basis functions with minimal overlapping support in the real-valued Hilbert space $L^2(\Omega^{\alpha},\mathbb{R})$, equipped with the inner product $[f,g] = \int_{\Omega^{\alpha}} f(z)g(z)\,\mathrm{d}z$. The set $\{\beta^{\alpha}_{n}\}$ consists of independent one-dimensional real-valued Brownian motions. Furthermore, the two sets of Brownian motions, $\{\beta^{o}_{n}\}$ and $\{\beta^{a}_{n}\}$, are assumed to be independent, as they correspond to stochastic processes arising from distinct physical media, namely the atmosphere and the ocean.

Given the anti-derivative of the horizontal Stokes drift, defined as $\mathbf{U}^{\alpha}_{s}(z) = \int_{H^o}^{z} \mathbf{u}^{\alpha}_{s}(\zeta)\,\mathrm{d}\zeta$, where $\mathbf{u}^{\alpha}_{s}(z) = u^{\alpha}_{s}(z) + i v^{\alpha}_{s}(z)$, the horizontal noise component can be constructed as

$$\boldsymbol{\sigma}^{\alpha}_{\mathbf{x}}\,\mathrm{d}B^{\alpha}_{t} = \sqrt{2}\sum_{n>0}\big[(a^{\alpha}_{zz})^{-1/2}\mathbf{U}^{\alpha}_{s}, e^{\alpha}_{n}\big](t)\, e^{\alpha}_{n}(z)\,\mathrm{d}\beta^{\alpha}_{n}(t), \tag{2.3b}$$

where the inner product is interpreted as $[\mathbf{U}, e_n] = [U, e_n] + i[V, e_n]$.

It is typically assumed that the Stokes drift is not included in the atmospheric momentum equation [Lewis and Belcher, 2004], as it is generally much smaller than the geostrophic wind. In the following, we neglect $\mathbf{u}^{a}_{s}$ by assuming negligible atmospheric horizontal noise ($\boldsymbol{\sigma}^{a}_{\mathbf{x}}\,\mathrm{d}B^{a}_{t} \approx 0$) and refer to the Stokes drift $\mathbf{u}_s$ exclusively in the ocean. As a result, the stochastic atmospheric Ekman model simplifies to:

$$\mathrm{d}\mathbf{u}^{a} = \Big(-if\big(\mathbf{u}^{a} - \mathbf{u}^{a}_{g}\big) + \partial_z\big(\nu^{a}\partial_z\mathbf{u}^{a}\big)\Big)\,\mathrm{d}t - \sigma^{a}_{z}\partial_z\mathbf{u}^{a}\,\mathrm{d}B^{a}_{t}. \tag{2.4}$$

Taking the expectation, the mean wind velocity $\mathbb{E}[\mathbf{u}^{a}]$ satisfies

$$\partial_t\mathbb{E}[\mathbf{u}^{a}] = -if\Big(\mathbb{E}[\mathbf{u}^{a}] - \mathbf{u}^{a}_{g}\Big) + \partial_z\Big(\mathbb{E}\big[\nu^{a}\partial_z\mathbf{u}^{a}\big]\Big), \tag{2.5}$$

where the last term is generally nonlinear, as the turbulent viscosity closure for a^{a}_{zz} (recalling that $\nu^{a} = \nu^{a}_{m} + a^{a}_{zz}$) typically depends on the pathwise solution $\mathbf{u}^{a}$, at least through air-sea coupling, as will be demonstrated later. The stochastic model (2.4) can therefore be interpreted as a generalization of the classical model, incorporating random fluctuation effects arising from unresolved smaller scales.

Similarly, taking the expectation of Eq. (2.1a) for the ocean component, the mean current velocity $\mathbb{E}[\mathbf{u}^{o}]$ satisfies

$$\partial_t\mathbb{E}[\mathbf{u}^{o}] = -if\Big(\mathbb{E}[\mathbf{u}^{o}] + \mathbb{E}[\mathbf{u}_s] - \mathbf{u}^{o}_{g}\Big) + \partial_z\Big(\mathbb{E}\big[\nu^{o}\partial_z\mathbf{u}^{o}\big] + \mathbb{E}\big[\nu^{o}\partial_z\mathbf{u}_s\big]\Big), \tag{2.6}$$

which remains a nonlinear equation – because of the dependency of μ^o on $\mathbf{u}^o$. In general, the Stokes drift may also exhibit stochastic variability, as will be shown later. Unlike the classical Ekman-Stokes model, which accounts only for the Coriolis-Stokes force $if\mathbb{E}[\mathbf{u}_s]$, the proposed mean model introduces an additional term, $\partial_z\big(\mathbb{E}[\nu^o\partial_z\mathbf{u}_s]\big)$, representing a *wave mixing* effect. This term initially arises from a change of variables in the derivation of the generalized stochastic Craik-Leibovich equation [Bauer et al., 2020].

To further examine its influence, one can vertically integrate the mean current velocity. The mean current transport, given by $\mathbb{E}[\mathbf{T}^o] = \int_{\hat{\Omega}^o}\mathbb{E}[\mathbf{u}^o](z)\,\mathrm{d}z$, then satisfies

$$\partial_t\mathbb{E}[\mathbf{T}^o] = -if\Big(\mathbb{E}[\mathbf{T}^o] + \mathbb{E}[\mathbf{T}_s] - \mathbf{T}_g^o\Big) + \frac{1}{\rho^o}\Big(\mathbb{E}[\boldsymbol{\tau}] + \mathbb{E}[\boldsymbol{\tau}_s]\Big), \tag{2.7}$$

where $\boldsymbol{\tau}_s = \rho^o\nu^o\partial_z\mathbf{u}_s(\delta^o)$ represents an additional surface wave stress absent in the classical Ekman-Stokes model.

Returning to the general case, the SCESM (2.1), combined with the simplified atmospheric equation (2.4) and the specific noise representations (2.3), establishes a coupled framework for the atmospheric and oceanic boundary layers, incorporating both surface wave effects and random turbulent fluctuations. However, the SCESM does not account for stratification (buoyancy) effects, which will be investigated in future work. To complete the model, we present parameterizations for the air-sea momentum flux $\boldsymbol{\tau}$, the turbulent viscosity a_{zz}^{α}, and the Stokes drift $\mathbf{u}_s$ in the subsequent sections, all of which are based on well-established approaches.

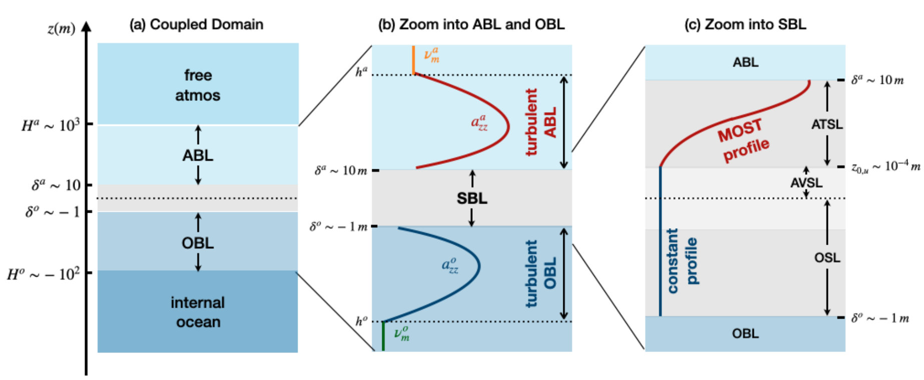

Fig. 1. Schematic representation of the one-dimensional coupled model configuration (inspired by Pelletier et al. [2021]). The model includes the atmospheric boundary layer (ABL), oceanic boundary layer (OBL), and surface boundary layer (SBL). The surface layer is further divided into the ocean surface layer (OSL), atmospheric viscous sub-layer (AVSL), and atmospheric turbulent sub-layer (ATSL).

2.2 Bulk parameterization of turbulent air-sea fluxes

In this section, we briefly review the parameterization of turbulent fluxes for the ocean-atmosphere coupling. We begin by recalling the atmospheric surface boundary layer model, which follows the Monin-Obukhov similarity theory (MOST) [Monin and Obukhov, 1954], a generalized law of the wall for stratified fluids (see [Pelletier et al., 2021] for a detailed introduction on the subject). Under the assumption of constant profiles in the ocean surface layer, the resolved wind $\mathbf{u}$, potential temperature θ and humidity q at the atmospheric surface layer depth δ^a, can be expressed in terms of their fundamental turbulent scales (u_*, θ_*, q_*), as follows:

$$\left|[\mathbf{u}]_{\delta^o}^{\delta^a}\right| = \frac{u_*}{\kappa}\left(\ln\Big(\frac{\delta^a}{z_{0,u}(u_*,\theta_*,q_*)}\Big) - \psi_m\Big(\frac{\delta^a}{L_O(u_*,\theta_*,q_*)}\Big)\right), \tag{2.8a}$$

$$[\theta]_{\delta^o}^{\delta^a} = \frac{\theta_*}{\kappa}\left(\ln\Big(\frac{\delta^a}{z_{0,\theta}(u_*,\theta_*,q_*)}\Big) - \psi_h\Big(\frac{\delta^a}{L_O(u_*,\theta_*,q_*)}\Big)\right), \tag{2.8b}$$

$$[q]_{\delta^o}^{\delta^a} = \frac{q_*}{\kappa}\left(\ln\Big(\frac{\delta^a}{z_{0,q}(u_*,\theta_*,q_*)}\Big) - \psi_h\Big(\frac{\delta^a}{L_O(u_*,\theta_*,q_*)}\Big)\right), \tag{2.8c}$$

where $[X]_{\delta^o}^{\delta^a} = X(\delta^a) - X(\delta^o)$ denotes the sea-surface-relative (under the ocean constant profiles assumption) value of the atmospheric quantity X, while $\kappa \approx 0.4$ is the von Kármán constant, $z_{0,u}$, $z_{0,\theta}$ and $z_{0,q}$ represent the surface roughness lengths for momentum, heat, and humidity, respectively. These roughness lengths depend on the turbulent scales. Additionally, L_O is the Obukhov length, which also depends on the turbulent scales, and ψ_m and ψ_h are the stability functions for momentum and tracer. The explicit forms of these functions can be found in Beljaars and Holtslag [1991], Grachev et al. [2000]. For the neutral case (without stratification), the above relationships reduce to the classical law of the wall, which is simply a logarithmic profile.

The Obukhov length L_O depends on the friction velocity scale u_* and the atmospheric buoyancy flux scale B_f as follows:

$$L_O = \frac{u_*^3}{\kappa B_f}, \qquad B_f = g u_* \left(\frac{\theta_*}{\theta_v(\delta_a)} + \frac{q_*}{q(\delta_a) + q_0}\right), \tag{2.9}$$

where $g \approx 9.81$ m s^{-2} is the gravity acceleration, $\theta_v(z) = \theta(z)\big(1 + q(z)/q_0\big)$ is the virtual potential temperature, and $q_0 \approx 0.61$ kg kg^{-1} is the specific humidity of saturated air.

Equations (2.8) are nonlinear, depending on the unknown turbulent scales (u_*, θ_*, q_*). To solve these three variables, a fixed-point iterative algorithm can be used. This numerical counterpart of the nonlinear formulation is referred to as the "bulk formula". Various versions exist, differing mainly in the initialization of the algorithm and the parameterization of surface roughness lengths. In this study, we adopt the well-established COARE (Coupled Ocean–Atmosphere Response Experiment) algorithm [Fairall et al., 1996, 2003].

Using the COARE algorithm, the wind stress $\boldsymbol{\tau}$, the sensible heat flux Q_{SH}, and the latent heat flux Q_{LH} across the air-sea interface are given by

$$|\boldsymbol{\tau}| = \rho^a C_d U \big|[\mathbf{u}]_{\delta^o}^{\delta^a}\big| = \rho^a u_*^2 \big|[\mathbf{u}]_{\delta^o}^{\delta^a}\big|/U, \tag{2.10a}$$

$$Q_{SH} = \rho^a c_P C_h U [\theta]_{\delta^o}^{\delta^a} = \rho^a c_P u_* \theta_*, \tag{2.10b}$$

$$Q_{LH} = \rho^a l_E C_e U [q]_{\delta^o}^{\delta^a} = \rho^a l_E u_* q_*, \tag{2.10c}$$

where c_P is the specific heat of air and l_E is the latent heat of vaporization. The transfer coefficients (C_d, C_h, C_e) for momentum, heat and humidity all depend on the turbulent scales (u_*, θ_*, q_*), and are determined from the equations above:

$$C_d = \left(\frac{\kappa}{\ln(\delta_a/z_{0,u}) - \psi_m(\delta_a/L)} \right)^2, \tag{2.11a}$$

$$C_h = \frac{\kappa C_d^{1/2}(\delta_a)}{\ln(\delta_a/z_{0,\theta}) - \psi_h(\delta_a/L)}, \tag{2.11b}$$

$$C_e = \frac{\kappa C_d^{1/2}(\delta_a)}{\ln(\delta_a/z_{0,q}) - \psi_h(\delta_a/L)}. \tag{2.11c}$$

In Eqs. (2.10), U denotes the scale the scalar difference in velocity across the air-sea interface, incorporating a "gustiness" factor u_{gust}, defined as

$$U = \left(\big|[\mathbf{u}]_{\delta^o}^{\delta^a}\big|^2 + u_{\text{gust}}^2 \right)^{1/2}, \tag{2.12a}$$

$$u_{\text{gust}} = \begin{cases} 1.2(B_f z_i)^{1/3}, & \text{if } B_f > 0 \\ 0.2, & \text{if } B_f \le 0, \end{cases} \tag{2.12b}$$

where $z_i \approx 600$ m is the convective boundary layer depth. The gustiness parameter accounts for atmospheric stability and is included in the COARE algorithm to ensure non-zero momentum fluxes at low wind speeds, by parameterizing the convective effect on momentum transfer.

Finally, the surface roughness lengths are parameterized in COARE by

$$z_{0,u} = \alpha_{ch} \frac{u_*^2}{g} + 0.11 \frac{\nu_m^a}{u_*}, \tag{2.13a}$$

$$z_{0,\theta} = \min\left(1.15 \times 10^{-4}, 5.5 \times 10^{-5} R_r^{-0.6}\right), \qquad R_r = z_{0,u} \frac{u_*}{\nu_m^a}, \tag{2.13b}$$

$$z_{0,\theta} = z_{0,q}. \tag{2.13c}$$

The momentum roughness in (2.13a) is separated into a rough-flow component using Charnock scaling [Charnock, 1955] and a smooth-flow component with a fixed roughness Reynolds number. The Charnock coefficient α_{ch} can be parameterized in different ways to account for physical effects. One such approach, based on wind speed [Fairall et al., 2003], uses a piecewise increasing and affine function of U:

$$\alpha_{ch}(U) = \begin{cases} 0.011, & \text{if } U \leq 10\,\text{m s}^{-1} \\ 0.011 + 0.007(U-10)/8, & \text{if } U \in (10,18)\,\text{m s}^{-1} \\ 0.018, & \text{if } U \geq 18\,\text{m s}^{-1}. \end{cases} \tag{2.14a}$$

Alternatively, the Charnock coefficient can be parameterized as a function of wave age [Maat et al., 1991]:

$$\alpha_{ch}(u_*, C_p) = A\left(\frac{u_*}{C_p}\right)^B, \tag{2.14b}$$

where C_p is the phase speed of the waves at the spectral peak. The constants $A = 0.114$ and $B = 0.622$ are used in COARE 3.5 [Edson et al., 2013].

Another approach is to parameterize surface roughness based on wave slope, as in the sea state– and wave age–dependent formulation [Donelan, 1990]:

$$\alpha_{ch}(u_*, C_p, H_s) = A'H_s\left(\frac{u_*}{C_p}\right)^{B'}\frac{g}{u_*^2}, \tag{2.14c}$$

where H_s is the significant wave height. The constants $A' = 0.091$ and $B' = 2$ are used in COARE 3.5 [Edson et al., 2013].

In this work, we employ the COARE (fixed-point) algorithm, using the relative wind $[\mathbf{u}]_{\delta^o}^{\delta^a}(t)$ at each time step, while maintaining fixed values for the potential temperature $[\theta]_{\delta^o}^{\delta^a}$ and specific humidity $[q]_{\delta^o}^{\delta^a}$. This allows us to first determine the turbulent scales (u_*, θ_*, q_*) along with the intermediate transfer coefficients (C_d, C_h, C_e). Consequently, the wind stress is given by $\boldsymbol{\tau}(t) = \rho^a\left(u_*^2[\mathbf{u}]_{\delta^o}^{\delta^a}/U\right)(t)$, which provides the surface boundary condition (2.1d) at each time step. This formulation assumes a stratified atmospheric surface layer, albeit with steady or time-averaged tracers, while considering the neutral SCESM (2.1). The heat fluxes in (2.10) will be incorporated in future investigations of stratified Ekman boundary layers, particularly when incorporating the evolution equations for temperature [McWilliams et al., 2009].

2.3 Turbulent viscosity closure and Stokes drift

In this work, we implement the diagnostic K-Profile Parameterization (KPP) scheme [Large et al., 1994] for turbulent viscosity closure. The KPP scheme, consistent with the MOST, is formulated in a nondimensional vertical coordinate $\zeta^\alpha = |z|/h^\alpha$, where h^α represents the turbulent boundary layer depth. The general formulation is expressed as:

$$a_{zz}^\alpha(\zeta^\alpha) = h^\alpha w(\zeta^\alpha)G(\zeta^\alpha), \qquad w(\zeta^\alpha) = \frac{\kappa u_*}{\phi_m(\zeta h^\alpha/L_O)}, \tag{2.15}$$

where w is the turbulent vertical velocity scale and G is a fourth-order polynomial [Large et al., 1994], ensuring that the viscosity and its gradient match specific values at the top and bottom of the boundary layer. The universal function ϕ_m is set to unity for neutral conditions, simplifying the formulation to match the profiles of O'Brien [1970].

In the stratified case, the boundary layer depth h^α depends on both velocity and buoyancy, with the bulk Richardson number [Large et al., 1994] governing the relationship. In the particular case of neutral conditions, the Ekman layer depth is defined by:

$$h^\alpha(t) = \frac{c^\alpha}{|f|} u_*(t), \tag{2.16}$$

where the atmospheric constant $c^a = 0.2$ Arya [1981] and the oceanic constant $c^o = -0.7$ Large et al. [1994] are used. These constants are consistent with the MOST.

It is worth noting that a prognostic turbulence scheme, based on the generic length scale theory [Umlauf and Burchard, 2003], and specifically second-moment closure [Harcourt, 2013, 2015] for Langmuir turbulence, which solves a turbulent kinetic energy (TKE) equation, could be explored in future studies following a similar framework.

In general, surface gravity waves exhibit a broad spectrum, leading to a complex vertical profile for the Stokes drift [Huang, 1971, Jenkins, 1989]. For simplicity, we consider a steady, monochromatic deep-water wave in this study. The surface elevation, accurate to the leading order in wave steepness, is expressed as $\eta = \eta_0 \cos(kx - \omega t)$, where η_0 is the wave amplitude, k is the horizontal wavenumber, and $\omega = (gk)^{1/2}$ is the angular frequency, consistent with the deep-water dispersion relation. The corresponding horizontal components of the Stokes drift are approximated by Phillips [1977] as:

$$\mathbf{u}_s(z) = U_s e^{2kz} e^{i\theta_s}, \tag{2.17}$$

where $U_s = \omega k \eta_0^2$ is the magnitude of the Stokes drift, and θ_s represents the wave propagation direction. Following Li et al. [2024], the wave direction θ_s is parameterized by a normal distribution: $\theta_s \sim \mathcal{N}(\Theta_s, \Sigma_s)$, where the mean direction Θ_s is aligned with the geostrophic wind, and the small standard deviation Σ_s represents the angular uncertainty, accounting for the misalignment between wind and wave direction.

Note that the anti-derivative $\mathbf{U}_s$, used in Eq.(2.3b) for the Stokes drift profile, is given by $\mathbf{u}_s/(2k)$. For the monochromatic wave described in Eq.(2.17), the phase speed of the waves at the spectral peak and the significant wave height, used in the wave-age dependent formulation (2.14b) and (2.14c) for surface roughness parameterization, are defined as [McWilliams et al., 2014]:

$$C_p = \omega/k = \sqrt{g/k}, \qquad H_s = 2\sqrt{2}\eta_0. \tag{2.18}$$

3 Results

In this section, we numerically investigate the proposed stochastic coupled Ekman-Stokes model (SCESM) with the presented parameterization through ensemble simulations.

3.1 Model configurations

The configuration parameters are presented in Table 1, with most values selected to be consistent with the observational data discussed later. The SCESM is solved numerically using a pseudo-spectral Chebyshev method combined with an implicit time-stepping scheme [Li et al., 2024]. The ocean and atmosphere domains are discretized with 300 and 1000 Chebyshev nodes, respectively, and 500 ensemble members are used. The coupled model is integrated for 20 days using a uniform time step of $\Delta t^a = \Delta t^o = 300$ s to integrate the coupled model for 20 days. Air-sea coupling is applied at each time step using the instantaneous surface wind and current. While this approach may not be entirely realistic, it can be improved in future work using asynchronous/synchronous coupling methods [Valcke, 2021] with a larger ocean time step than the atmosphere, or by employing the Schwarz iterative method [Marti et al., 2021].

Table 1. Model Parameters

Symbol	Value	Description
H^a	1000 m	Upper bound of atmospheric domain
H^o	-100 m	Lower bound of oceanic domain
δ^a	10 m	Lower bound of atmospheric domain
δ^o	-1 m	Upper bound of oceanic domain
f	8.36×10^{-5} s^{-1}	Coriolis parameter
ν_m^a	1.5×10^{-5} m^2 s^{-1}	Air kinematic viscosity
ν_m^o	10^{-6} m^2 s^{-1}	Water kinematic viscosity
ρ^o	10^3 kg m^{-3}	Water density
ρ^a	1 kg m^{-3}	Air density
$\mathbf{u}_g^a$	$(9 + 0i)$ m s^{-1}	Geostrophic wind velocity
$\mathbf{u}_g^o$	0 m s^{-1}	Geostrophic current velocity
$\theta^a(\delta^a)$	299.65 K (26.5°C)	Atmospheric potential temperature at δ^a
$\theta^o(\delta^o)$	301.15 K (28°C)	Oceanic potential temperature at δ^o
$q(\delta^a)$	0%	Atmospheric specific humidity at δ^a
η_0	0.8 m	Surface wave amplitude
λ	60 m	Wavelength of surface wave
Θ_s	0°	Wave mean propagation direction
Σ_s	5°	Wave spreading angle

To assess the contributions of different modeling terms in the SCESM, we compare it against several reduced versions:

- **RAM**: Stochastic atmosphere model coupled with a deterministic ocean model without Stokes drift:

$$\mathrm{d}\mathbf{u}^a = \Big(-if\big(\mathbf{u}^a - \mathbf{u}_g^a\big) + \partial_z\big(\nu^a \partial_z \mathbf{u}^a\big)\Big)\,\mathrm{d}t - \sigma_z^a \partial_z \mathbf{u}^a \,\mathrm{d}B_t^a, \tag{3.1a}$$

$$\partial_t \mathbf{u}^o = -if\big(\mathbf{u}^o - \mathbf{u}_g^o\big) + \partial_z\big(\nu^o \partial_z \mathbf{u}^o\big). \tag{3.1b}$$

- **ROM**: Deterministic atmosphere model coupled with a stochastic ocean model without Stokes drift:

$$\partial_t \mathbf{u}^a = -if\big(\mathbf{u}^a - \mathbf{u}_g^a\big) + \partial_z\big(\nu^a \partial_z \mathbf{u}^a\big), \tag{3.2a}$$

$$\mathrm{d}\mathbf{u}^o = \Big(-if\big(\mathbf{u}^o - \mathbf{u}_g^o\big) + \partial_z\big(\nu^o \partial_z \mathbf{u}^o\big)\Big)\,\mathrm{d}t - \sigma_z^o \partial_z \mathbf{u}^o \,\mathrm{d}B_t^o. \tag{3.2b}$$

- **RCM**: Stochastic atmosphere model (3.1a) coupled with a stochastic ocean model (3.2b) without Stokes drift.
- **RCM-RS**: RCM with Stokes drift under random angular directions, but without wave mixing terms. That is, Eq. (3.1a) with

$$\mathrm{d}\mathbf{u}^o = \Big(-if\big(\mathbf{u}^o + \mathbf{u}_s - \mathbf{u}_g^o\big) + \partial_z\big(\nu^o \partial_z \mathbf{u}^o\big)\Big)\,\mathrm{d}t - \Big(\sigma_z^o \partial_z \mathbf{u}^o + if\boldsymbol{\sigma}_{\mathbf{x}}^o\Big)\,\mathrm{d}B_t^o. \tag{3.3}$$

- **RCM-RS-WM**: RCM-RS with wave mixing terms. That is, Eq. (3.1a) with

$$\begin{aligned}\mathrm{d}\mathbf{u}^o = \Big(&-if\big(\mathbf{u}^o + \mathbf{u}_s - \mathbf{u}_g^o\big) + \partial_z\big(\nu^o \partial_z (\mathbf{u}^o + \mathbf{u}_s)\big)\Big)\,\mathrm{d}t \\ &- \Big(\sigma_z^o \partial_z \big(\mathbf{u}^o + \mathbf{u}_s\big) + if\boldsymbol{\sigma}_{\mathbf{x}}^o\Big)\,\mathrm{d}B_t^o.\end{aligned} \tag{3.4}$$

All models are initialized with the same initial condition (2.1b) and use the same Dirichlet boundary condition (2.1c).

To distinguish the impact of different modeling terms from that of parameterization choices, we first conduct a comparative analysis using the same wind speed-dependent formulation (2.14a) for the surface roughness length. This ensures that the air-sea flux condition (2.1d) remains consistent across models.

For example, Fig. 2 demonstrates that all models yield similar ensemble mean values for the friction velocity u_* and the air-sea momentum transfer coefficient C_d, with RCM-RS and RCM-RS-WM exhibiting slight increases in these values. Additionally, the overall level of uncertainty is similar across models, except for ROM, which explicitly incorporates stochasticity only in the ocean. Unsurprisingly, this significantly reduces the uncertainty representation of air-sea fluxes.

In this context, we first compare the model performances against observations in Section 3.2, followed by a statistical analysis of model diagnostics in Section 3.3. Additional results incorporating wave-dependent formulations (2.14b) and (2.14c) for RCM-RS and RCM-RS-WM are presented in Section 3.4.

3.2 Comparison with LOTUS observations

To assess the models' performance, we compare their outputs with observations from the Long-Term Upper-Ocean Study (LOTUS) experiment [Price et al., 1987, Price and Sundermeyer, 1999], conducted in the western Sargasso Sea (34°N, 70°W) during the summer of 1982. This dataset provides 160 days of current profile measurements collected using vector-measuring instruments mounted on a stable platform to mitigate errors associated with mooring motion. The geostrophic velocity, assumed constant at a depth of 50 m, was removed to

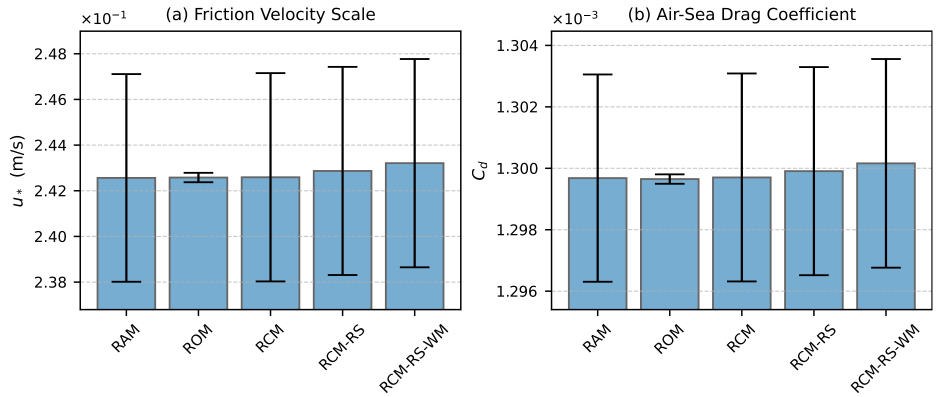

Fig. 2. Comparison of the ensemble mean (represented by bars) and spread (represented by error bars) for (a) friction velocity u_* and (b) air-sea momentum transfer coefficient C_d, across different random models (labeled on the x-axis). The ensemble mean and spread ($\text{mean}(u) \pm \text{std}(u)$) are time-averaged over the last 10 days.

extract the wind-driven signal. Wind and current data were daily averaged to reduce high-frequency oscillations in the observed signals, rotated to align the wind direction with nominal north, and subsequently averaged over the 160-day period. Table 1 in Price et al. [1987] reports the mean values and confidence intervals for the downwind and crosswind current components at depths $z = (-5, -10, -15, -25)$ m.

To ensure comparability with observations, the model's eastward and northward ocean velocity components (u^o and v^o) on the wind-relative coordinates are rotated into a wind-relative coordinate system. The downwind and crosswind velocity components, $u_\parallel$ and $u_\perp$, are defined as

$$\begin{pmatrix} u_\parallel \\ u_\perp \end{pmatrix} = \begin{pmatrix} \cos(\theta) & \sin(\theta) \\ \sin(\theta) & -\cos(\theta) \end{pmatrix} \begin{pmatrix} u^o \\ v^o \end{pmatrix}, \qquad \theta = \arg(\boldsymbol{\tau}). \tag{3.5}$$

This rotation is applied to each random realization of the model outputs $\mathbf{u}^o$ and τ, without performing daily averaging of the data. We retain the full dataset to compute ensemble statistics before applying low-pass filtering or time-averaging for visualization.

Fig. 3 qualitatively compares the ensemble mean and spread (defined as mean $\pm$ standard deviation) of the Ekman current profiles for different random models, alongside the mean and confidence intervals (CIs) of the observations. It shows that the RAM, which introduces explicit stochastic transport only in the atmosphere, produces a very low ensemble spread and fails to both encompass the mean of the observations and overlap with their CIs over depth. The ROM and RCM, which incorporate explicit stochastic transport in the ocean, increase the spread but still fail to align with the observations near the surface, particularly at $z = (-5, -10)$ m. The RCM-RS and RCM-RS-WM, which include the

Coriolis-Stokes force, modify the shape of the current profiles and overlap most of the observation CIs across depth, particularly near the surface. Compared to the other random models, the RCM-RS-WM, which includes additional wave mixing effects, significantly increases the spread over depth and shifts the spread to the left for the downwind component and to the right for the crosswind component.

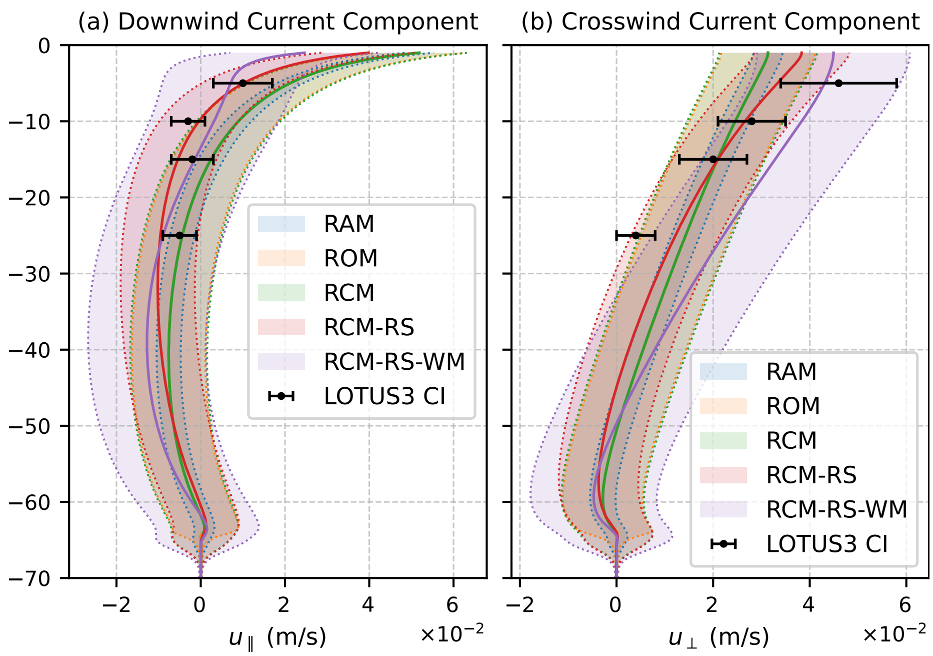

Fig. 3. Comparison of the ensemble mean (solid lines) and spread (shaded areas) for (a) downwind Ekman current and (b) crosswind Ekman current across different random models. These are compared to the confidence interval (CI, represented by black error bars) of the mean (centered point) LOTUS3 observations (Table 1 of Price et al. [1987]) at near-surface depths. The ensemble mean and spread ($\text{mean}(u) \pm \text{std}(u)$) are time-averaged over the last 10 days.

To further evaluate the models' performance against the LOTUS observations, we employ statistical metrics that account for observational uncertainties. Specifically, we generate observation samples following normal distributions, $u_\parallel^{\text{obs}} \sim \mathcal{N}\left(\widehat{\mu}_\parallel, \widehat{\sigma}_\parallel^2\right)$ and $u_\perp^{\text{obs}} \sim \mathcal{N}\left(\widehat{\mu}_\perp, \widehat{\sigma}_\perp^2\right)$, where the mean values $\widehat{\mu}$ and the standard errors $\widehat{s} = \alpha\widehat{\sigma}/\sqrt{n}$ are obtained from Table 1 of Price et al. [1987]. The CI is given by $\text{CI} = [\widehat{\mu} - \widehat{s}, \widehat{\mu} + \widehat{s}]$, where $n = 53$ represents the effective degrees of freedom used to estimate the standard error over the 160-day record. The confidence levels are set to 95% ($\alpha = 2$) for the downwind component and 90%

($\alpha = 1.7$) for the crosswind component. The corresponding sample standard deviations, $\widehat{\sigma}_{\parallel}$ and $\widehat{\sigma}_{\perp}$, are derived from these values.

We employ two statistical metrics for the model comparison. The first is the Wasserstein distance [Villani, 2009], which quantifies the similarity between two probability distributions. Specifically, we use the empirical cumulative distribution functions, $\widehat{F}_{X_e}$ and $\widehat{F}_{X_o}$, of the model ensemble X_e and the randomly generated observations X_o, respectively, to compute the p-th order Wasserstein distance estimator:

$$\widehat{W}_p(X_e, X_o) = \left(\int_{\mathbb{R}} \left| \widehat{F}_{X_e}(x) - \widehat{F}_{X_o}(x) \right|^p \mathrm{d}x \right)^{1/p}. \tag{3.6}$$

The second metric is the continuous ranked probability score (CRPS) [Weigel, 2011], which evaluates ensemble forecast skill by measuring the integrated squared difference between the cumulative forecast and the observation. In this work, for each realization of the random observations, $x_o^{(i)},\ i = 1, \ldots, n$, the CRPS is computed as

$$\mathrm{CRPS}\left(\widehat{F}_{X_e}, x_o^{(i)}\right) = \int_{\mathbb{R}} \left(\widehat{F}_{X_e}(x) - \mathrm{H}\big(x - x_o^{(i)}\big) \right)^2 \mathrm{d}x, \tag{3.7a}$$

where H is the Heaviside step function. The final CRPS score is obtained by averaging over all sampled observations:

$$\overline{\mathrm{CRPS}} = \frac{1}{n} \sum_{i=1}^{n} \mathrm{CRPS}\left(\widehat{F}_{X_e}, x_o^{(i)}\right). \tag{3.7b}$$

To compute these metrics, we independently draw observation samples (following the normal distributions described above) for each time step and depth. The scores are then averaged over depth, yielding time series of the scores for each model. A lower score indicates better model performance.

Fig. 4 presents the temporal evolution of the globally integrated first-order ($p = 1$) Wasserstein distance and the mean globally integrated CRPS for each model ensemble against LOTUS observations. The results clearly demonstrate an increasing order of model performance:

$$\text{RAM} < \text{ROM} < \text{RCM} < \text{RCM-RS} < \text{RCM-RS-WM}.$$

This ranking quantifies the contribution of each additional modeling term in the fully coupled stochastic system to the overall improvement of the model.

3.3 Statistical diagnostics of energy budget and wind work

We begin by analyzing the ensemble decomposition of global energy for both atmospheric and oceanic components, specifically the mean kinetic energy (MKE) and eddy kinetic energy (EKE). The MKE is defined as $\mathrm{MKE}^{\alpha} = \rho^{\alpha} \|\overline{\mathbf{u}^{\alpha}}\|^2$,

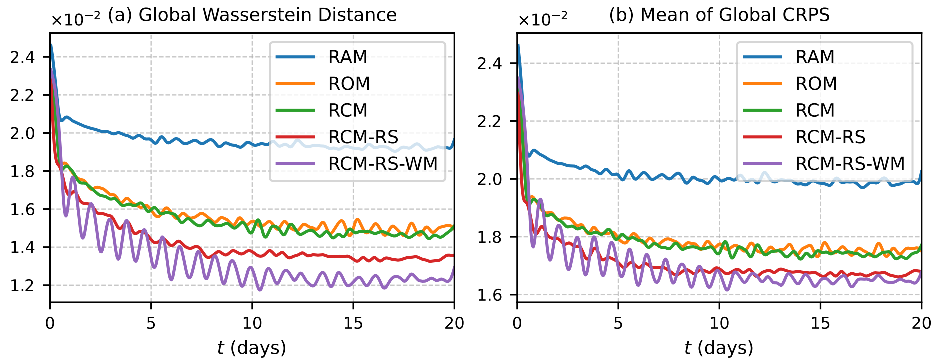

Fig. 4. Comparison of (a) the globally integrated Wasserstein distance and (b) the mean globally integrated continuous ranked probability score (CRPS) over time for different model ensembles against LOTUS3 observations. Observation samples are drawn from a normal distribution with empirical mean and standard deviation derived from Table 1 of Price et al. [1987]. At each time, the CRPS is computed using an observation realization and averaged over samples. A half-day low-pass filter is applied to these time series.

while the EKE is given by $\mathrm{EKE}^\alpha = \rho^\alpha \overline{\|\mathbf{u}^\alpha - \overline{\mathbf{u}^\alpha}\|^2}$, where $\overline{u}$ denotes the ensemble mean of u. Fig. 5(c) shows that all models exhibit similar time-mean values of MKE^a, albeit with varying levels of oscillation around their respective means. In contrast, Fig. 5(a) demonstrates that the RCM-RS-WM significantly increases the MKE^o compared to all the other random models, due to the inclusion of additional wave mixing terms.

As illustrated in Fig. 5(b), RAM, which introduces explicit stochastic transport only in the atmosphere, generates high EKE^a but very low EKE^o. Conversely, as shown in Fig. 5(d), ROM, which introduces explicit stochastic transport only in the ocean, produces high EKE^o but very low EKE^a. The RCM model, which incorporates explicit stochastic transport in both the atmosphere and ocean, yields EKE^o levels comparable to ROM and EKE^a levels similar to RAM. These results clearly indicate that explicitly representing uncertainties in both components plays a crucial role in determining the variance levels of a coupled system. Furthermore, the two wave-dependent models exhibit EKE^a levels similar to those of RCM (Fig. 5d); however, the RCM-RS model slightly reduces EKE^o, whereas the RCM-RS-WM model significantly enhances it (Fig. 5c).

We next examine the wind contribution to the ensemble energy budget for both the atmosphere and ocean, characterized by the mean wind work $\mathrm{MWW}^\alpha = \overline{\boldsymbol{\tau}} \cdot \overline{\mathbf{u}^\alpha}(\delta^\alpha)$ and the eddy wind work $\mathrm{EWW}^\alpha = \overline{(\boldsymbol{\tau} - \overline{\boldsymbol{\tau}}) \cdot (\mathbf{u}^\alpha - \overline{\mathbf{u}^\alpha})(\delta^\alpha)}$. Fig. 6(a) indicates that surface waves significantly reduce the mean level of MWW^o over time while increasing its oscillation, as observed in the comparison of RCM-RS and RCM-RS-WM with RAM, ROM, and RCM. Furthermore, due to wave mixing effects, the reduction in MWW^o is more pronounced in RCM-RS-WM than in RCM-RS. Conversely, Fig. 6(c) illustrates that surface waves induce a

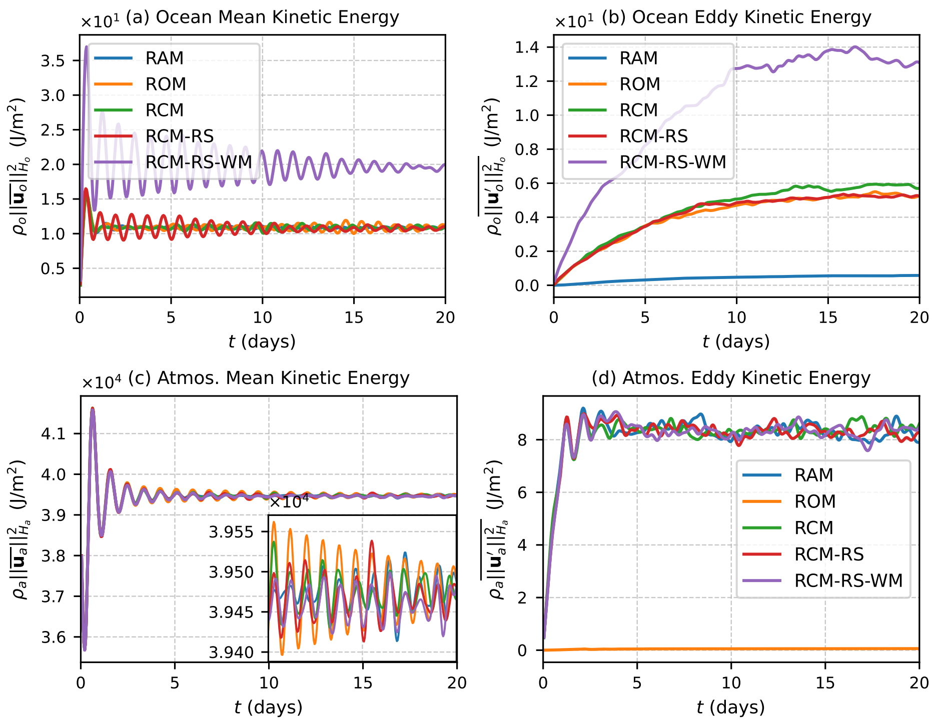

Fig. 5. Comparison of globally integrated mean kinetic energy (MKE, left) and eddy kinetic energy (EKE, right) for the ocean (top) and atmosphere (bottom) components across different random models (distinguished by color). MKE and EKE are defined in an ensemble sense as $\overline{\mathbf{u}} := \widehat{\mathbb{E}}[\mathbf{u}]$ and $\mathbf{u}' := \mathbf{u} - \widehat{\mathbb{E}}[\mathbf{u}]$. A half-day low-pass filter is applied to these time series. A zoomed-in view of atmospheric MKE over the last 10 days is included to better highlight the differences.

slight increase in the mean level of MWW^a, an effect that becomes more evident when wave mixing terms are included.

As expected, ROM, which lacks explicit atmospheric uncertainty representation, exhibits an almost negligible EWW^a and a small negative EWW^o, as shown in Figures 6(b) and (d). The other models exhibit similar levels of EWW^a (Fig. 6d). Additionally, the inclusion of wave mixing terms reduces the mean level of EWW^o over time while increasing its temporal variability (Fig. 6b).

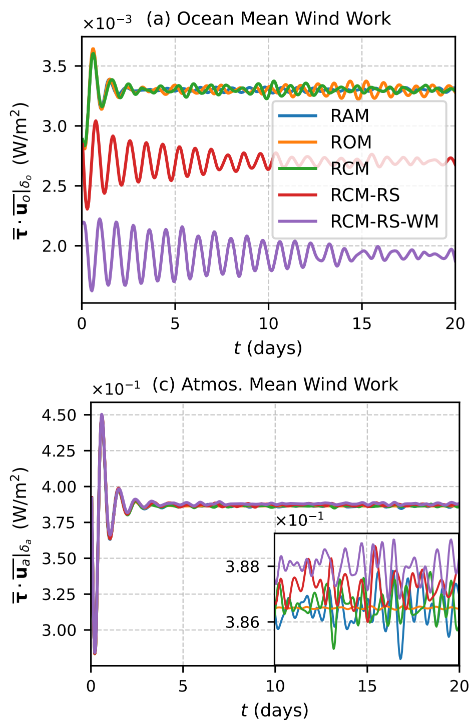

Fig. 6. Comparison of mean wind work (left) and eddy wind work (right) for the ocean (top) and atmosphere (bottom) components across different random models (distinguished by color).

3.4 Discussion of wave-dependent surface roughness effects

We now examine the results obtained using the wave-dependent parameterization of surface roughness length for RCM-RS and RCM-RS-WM. Specifically, we focus on their impact on model performance relative to observations, employing the same statistical metrics as those presented in Section 3.2.

When adopting the wave age-dependent formulation (2.14b), Fig. 7 illustrates that both the mean friction velocity and air-sea transfer coefficients increase compared to those obtained using the wind speed-dependent formulation (2.14a). In this case, Fig. 8 demonstrates that the model performance ranking established in Section 3.2,

$$\text{RAM} < \text{ROM} < \text{RCM} < \text{RCM-RS} < \text{RCM-RS-WM},$$

remains valid in terms of both the Wasserstein distance and CRPS. However, the relative improvement of RCM-RS-WM over RCM-RS is slightly less pronounced.

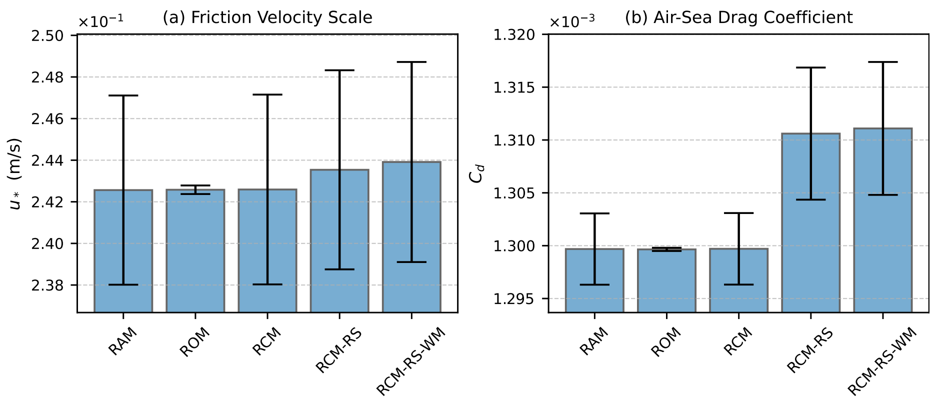

Fig. 7. Same as Fig. 2, but using the wave age-based roughness parameterization (2.14b) for RCM-RS and RCM-RS-WM.

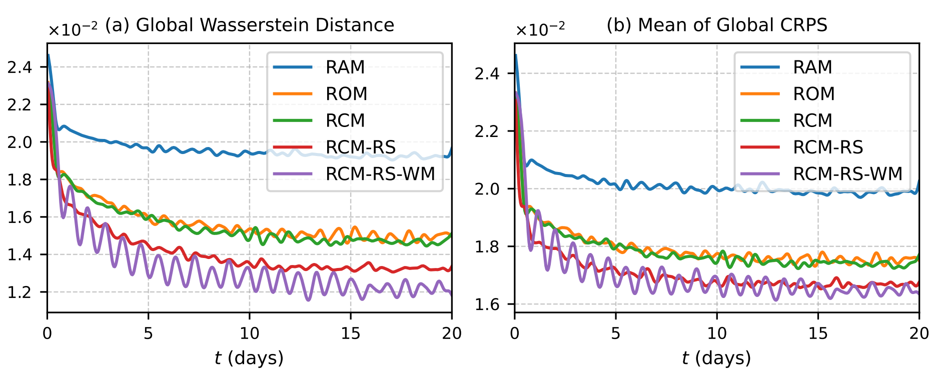

Fig. 8. Same as Fig. 4, but using the wave age-based roughness parameterization (2.14b) for RCM-RS and RCM-RS-WM.

For the wave slope-dependent formulation (2.14c), Fig. 9 indicates a more significant increase in air-sea fluxes compared to the wave age-based case. The model performance ranking remains consistent in this scenario, at least in terms of the Wasserstein distance. However, the improvement of RCM-RS-WM relative to RCM-RS is noticeably less pronounced than in the previous cases, suggesting that stronger air-sea fluxes diminish the relative contribution of wave mixing terms.

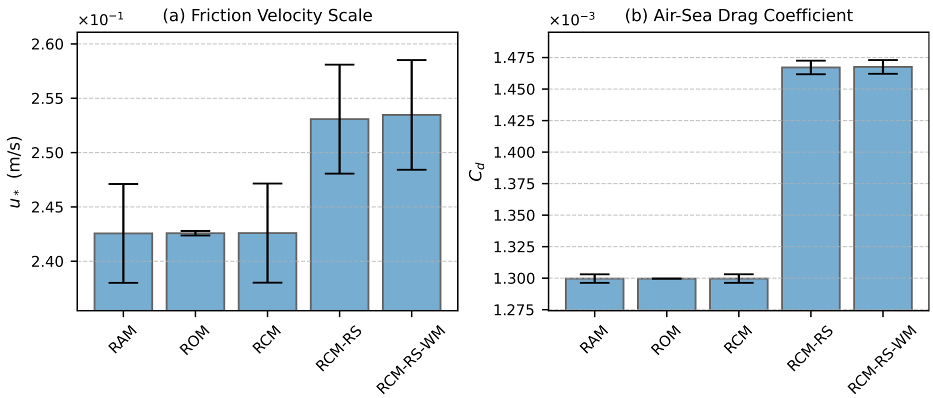

Fig. 9. Same as Fig. 2, but using the wave age-based roughness parameterization (2.14c) for RCM-RS and RCM-RS-WM.

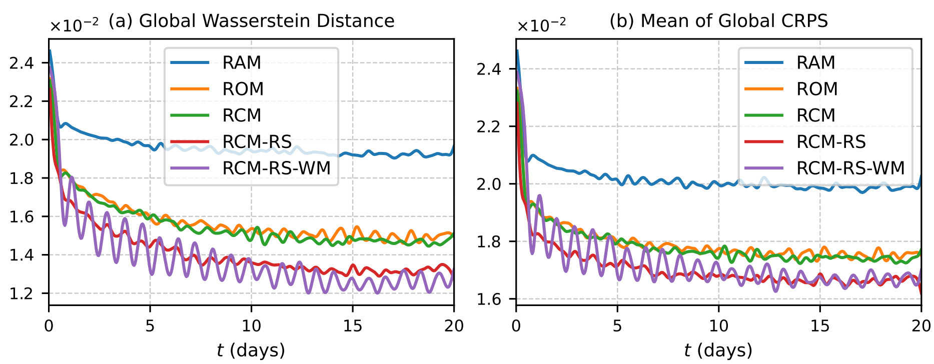

Fig. 10. Same as Fig. 4, but using the wave age-based roughness parameterization (2.14c) for RCM-RS and RCM-RS-WM.

4 Conclusion

We have introduced a stochastic coupled Ekman-Stokes model (SCESM) to represent the atmosphere-ocean boundary layers while incorporating surface wave effects and random turbulent fluctuations arising from unresolved scales. The SCESM, along with established parameterizations for air-sea fluxes, turbulent viscosity, and Stokes drift, was rigorously tested through ensemble simulations. Its performance was evaluated against LOTUS data using statistical metrics that account for observational uncertainties.

A performance ranking analysis quantified the impact of various modeling components within the fully coupled stochastic system. The results underscore the importance of explicitly representing uncertainties in both oceanic and atmospheric components to accurately capture the variance levels of the coupled system. Furthermore, while wave-dependent parameterizations of surface roughness enhance air-sea fluxes, they reduce the contribution of wave-induced mixing terms in the SCESM.

Looking ahead, several promising avenues for future research can be identified:

- **Modeling:** Extending the framework to account for buoyancy evolution driven by stochastic equations for stratified Ekman layers [McWilliams et al., 2009].
- **Parameterization:** Introducing memory effects in mixing through a TKE closure approach [Harcourt, 2013], adopting a two-sided surface layer parameterization for air-sea fluxes [Pelletier et al., 2021], and incorporating a spectral representation of surface waves with source terms and wave-induced momentum fluxes [Perrie et al., 2003].
- **Numerical Methods:** Improving the coupling algorithm by employing the Schwarz iterative method [Marti et al., 2021].

These developments hold the potential to refine the model's capabilities and address existing gaps in understanding coupled ocean-atmosphere dynamics.

Acknowledgments

The authors acknowledge the support of the ERC EU project 856408-STUOD.

Data availability statement

The PyTorch code **SCESM.py** used to reproduce the simulation data, along with the Python script **diag.py** which performs all diagnostics from the output data, and the Jupyter notebook **fig_stuod.ipynb** which generates the figures presented in this study, are available at https://github.com/matlong/SCESM.

Bibliography

S. Arya. Parameterizing the height of the stable atmospheric boundary layer. *J. Appl. Meteor. Climatol.*, 20(10):1192–1202, 1981.

W. Bauer, P. Chandramouli, B. Chapron, L. Li, and E. Mémin. Deciphering the role of small-scale inhomogeneity on geophysical flow structuration: a stochastic approach. *J. Phys. Oceanogr.*, 50(4):983–1003, 2020. doi: 10.1175/JPO-D-19-0164.1.

A. C. M. Beljaars and A. A. M. Holtslag. Flux parameterization over land surfaces for atmospheric models. *J. Appl. Meteor. Climatol.*, 30:327–341, 1991. doi: 10.1175/1520-0450(1991)030⟨0327:FPOLSF⟩2.0.CO;2.

R. Brecht, L. Li, W. Bauer, and E. Mémin. Rotating shallow water flow under location uncertainty with a structure-preserving discretization. *J. Adv. Model. Earth Syst.*, 13(12):e2021MS002492, 2021. doi: 10.1029/2021MS002492.

H. Charnock. Wind stress on a water surface. *Quart. J. Roy. Meteor. Soc.*, 81: 639–640, 1955. doi: 10.1002/qj.49708135027.

M. A. Donelan. *Air–sea interaction*, volume 9, page 239–292. Wiley and Sons, 1990.

J. B. Edson, V. Jampana, R. A. Weller, S. P. Bigorre, A. J. Plueddemann, C. W. Fairall, S. D. Miller, L. Mahrt, D. Vickers, and H. Hersbach. On the exchange of momentum over the open ocean. *J. Phys. Oceanogr.*, 43(8):1589–1610, 2013. doi: 10.1175/JPO-D-12-0173.1.

C. W. Fairall, E. F. Bradley, D. P. Rogers, J. B. Edson, and G. S. Young. Bulk parameterization of air-sea fluxes for tropical ocean-global atmosphere coupled-ocean atmosphere response experiment. *J. Geophys. Res.*, 101(C2): 3747–3764, 1996. doi: 10.1029/95JC03205.

C. W. Fairall, E. F. Bradley, J. E. Hare, A. A. Grachev, and J. B. Edson. Bulk parameterization of air–sea fluxes: Updates and verification for the COARE algorithm. *J. Climate*, 16:571–591, 2003. doi: 10.1175/1520-0442(2003)016⟨0571: BPOASF⟩2.0.CO;2.

A. A. Grachev, C. W. Fairall, and E. F. Bradley. Convective profile constants revisited. *Bound.-Lay. Meteorol.*, 94:495–515, 2000. doi: 10.1023/A: 1002452529672.

R. R. Harcourt. A second-moment closure model of Langmuir turbulence. *J. Phys. Oceanogr.*, 43(4):673–697, 2013. doi: 10.1175/JPO-D-12-0105.1.

R. R. Harcourt. An improved second-moment closure model of Langmuir turbulence. *J. Phys. Oceanogr.*, 45(1):84–103, 2015. doi: 10.1175/JPO-D-14-0046.1.

K. Hasselmann. Stochastic climate models Part I. Theory. *Tellus*, 28(6):473–485, 1976. doi: 10.1111/j.2153-3490.1976.tb00696.x.

N. E. Huang. Derivation of Stokes drift for a deep-water random gravity wave field. *Deep-Sea Res.*, 18(2):255–259, 1971. doi: 10.1016/0011-7471(71) 90115-X.

A. D. Jenkins. The use of a wave prediction model for driving a near- surface current model. *Dtsch. Hydrogr. Z.*, 42:134–149, 1989. doi: 10.1007/BF02226291.

W. G. Large, J. C. McWilliams, and S. C. Doney. Oceanic vertical mixing: A review and a model with a nonlocal boundary layer parameterization. *Rev. Geophys.*, 32(4):63–403, 1994. doi: 10.1029/94RG01872.

D. M. Lewis and S. E. Belcher. Time-dependent, coupled, Ekman boundary layer solutions incorporating Stokes drift. *Dyn. Atmos. Oceans*, 37(4):313–351, 2004. doi: 10.1016/j.dynatmoce.2003.11.001.

L. Li, B. Deremble, N. Lahaye, and E. Mémin. Stochastic data-driven parameterization of unresolved eddy effects in a baroclinic quasi-geostrophic model. *J. Adv. Model. Earth Syst.*, 15(2):e2022MS003297, 2023. doi: 10.1029/2022MS003297.

L. Li, E. Mémin, and B. Chapron. A generalized stochastic formulation of the Ekman-Stokes model with statistical analyses. Under Minor Revision in J. Phys. Oceanogr., https://hal.science/hal-04672188v2, 2024.

N. Maat, C. Kraan, and W. A. Oost. The roughness of wind waves. *Bound.-Lay. Meteorol.*, 54:89–103, 1991. doi: 10.1007/BF00119414.

A. J. Majda, I. Timofeyev, and E. Vanden Eijnden. Models for stochastic climate prediction. *Proc. Natl. Acad. Sci. (USA)*, 96(26):14687–14691, 1999. doi: 10.1073/pnas.96.26.14687.

O. Marti, S. Nguyen, P. Braconnot, S. Valcke, F. Lemarié, and E. Blayo. A Schwarz iterative method to evaluate ocean- atmosphere coupling schemes: Implementation and diagnostics in IPSL-CM6-SW-VLR. *Geosci. Model Dev.*, 14(5):2959–2975, 2021. doi: 10.5194/gmd-14-2959-2021.

J. C. McWilliams, E. Huckle, and A. F. Shchepetkin. Buoyancy effects in a stratified Ekman layer. *J. Phys. Oceanogr.*, 39(10):2581–2599, 2009. doi: 10.1175/2009JPO4130.1.

J. C. McWilliams, E. Huckle, J.-H. Liang, and P. P. Sullivan. Langmuir turbulence in swell. *J. Phys. Oceanogr.*, 44(3):870–890, 2014. doi: 10.1175/JPO-D-13-0122.1.

E. Mémin. Fluid flow dynamics under location uncertainty. *Geophys. Astrophys. Fluid Dyn.*, 108(2):119–146, 2014. doi: 10.1080/03091929.2013.836190.

A. S. Monin and A. M. Obukhov. Basic laws of turbulent mixing in the surface layer of the atmosphere. *Tr. Geofiz. Inst., Akad. Nauk SSSR*, 24:163–187, 1954.

J. J. O'Brien. A note on the vertical structure of the eddy exchange coefficient in the planetary boundary layer. *J. Atmos. Sci.*, 27(8):1213–1215, 1970.

T. N. Palmer. Stochastic weather and climate models. *Nat. Rev. Phys.*, 1: 463–471, 2019. doi: 10.1038/s42254-019-0062-2.

C. Pelletier, F. Lemarié, E. Blayo, M. N. Bouin, and J. L. Redelsperger. Two-sided turbulent surface-layer parameterizations for computing air–sea fluxes. *Quart. J. Roy. Meteor. Soc.*, 147(736):1726–1751, 2021.

W. Perrie, C. L. Tang, Y. Hu, and B. M. DeTracy. The impact of waves on surface currents. *J. Phys. Oceanogr.*, 33:2126–2140, 2003. doi: 10.1175/1520-0485(2003)033⟨2126:TIOWOS⟩2.0.CO;2.

O. M. Phillips. *The Dynamics of the Upper Ocean.* Cambridge University Press, 1977.

J. F. Price and M. A. Sundermeyer. Stratified Ekman layers. *J. Geophys. Res.*, 104(C9):20467–20494, 1999. doi: 10.1029/1999JC900164.

J. F. Price, R. A. Weller, and R. R. Schudlich. Wind-driven ocean currents and Ekman transport. *Science*, 238(4833):1534–1538, 1987. doi: 10.1126/science.238.4833.1534.

V. Resseguier, E. Mémin, and B. Chapron. Geophysical flows under location uncertainty, Part I, II & III . *Geophys. & Astro. Fluid Dyn.*, 111(3):149–227, 2017.

F. Tucciarone, L. Li, E. Mémin, and P. Chandramouli. Derivation and numerical assessment of a stochastic large-scale hydrostatic primitive model. Under Minor Revision in J. Adv. Model. Earth Syst., doi: 10.22541/essoar.173283035.57709416/v1, 2025.

L. Umlauf and H. Burchard. A generic length-scale equation for geophysical turbulence models. *J. Mar. Res.*, 61:235–265, 2003.

S. Valcke. *Coupling Algorithms and Specific Coupling Features in CGCMs*, chapter Chapter 9, pages 140–156. World Scientific Publishing Co., 2021. doi: 10.1142/9789811232947_0009.

C. Villani. *The Wasserstein distances*, pages 93–111. Springer Berlin Heidelberg, 2009. doi: 10.1007/978-3-540-71050-9_6.

A. P. Weigel. *Ensemble Forecasts*, chapter 8, pages 141–166. John Wiley & Sons, Ltd, 2011. doi: 10.1002/9781119960003.ch8.